PHYSICAL REVIEW B VOLUME 50, NUMBER 18 1 NOVEMBER 1994-II

Defect-induced Raman spectra in doped CeO_2

A. Nakajima,* A. Yoshihara, and M. Ishigame

Research Institute for Scientific Measurements, Tohoku University, 2-1-1 Katahira, Aoba-ku, Sendai 980, Japan

(Received 29 June 1994)

Polarized Raman-scattering spectra are obtained from oriented single crystals of yttria-doped CeO_2. The temperature and dopant dependencies of Raman spectra strongly suggest that many structures in the Raman spectra of yttria-doped CeO_2 are induced by the defect space including an O^{2-} vacancy. The contribution to the frequency distributions of Raman-active modes from the whole Brillouin zone are estimated from the imaginary part of the simple projection of the phonon displacement-displacement Green's functions of undoped CeO_2 crystals onto several defect spaces. The observed spectra are well explained by the linear combination of the calculated frequency distributions from the defect space consisting of the four metal ions and from that consisting of the six next-nearest-neighbor O^{2-} ions surrounding an O^{2-} vacancy. Brillouin-scattering spectra of CeO_2 are also measured in order to calculate the phonon-dispersion curves of CeO_2. The dependencies of type and concentration of defect space on dopant concentration in doped CeO_2 are also discussed.

I. INTRODUCTION

Some of the oxide having a fluorite-type structure, when doped with aliovalent cations, become good O^{2-} ion conductors at elevated temperatures. Stabilized ZrO_2 is one of the applicable materials among such fluorite-type oxides and is used as a solid electrolyte for oxygen sensors, fuel cells, etc.

Although the property of defect structures is extremely important in stabilized ZrO_2 in order to realize its ionic conduction mechanism, it is examined mainly at high defect concentrations because ZrO_2 cannot be stabilized to the fluorite structure at low dopant concentrations. However, to understand the essential characteristics of the defects in stabilized ZrO_2, it is necessary to study the structure and characteristics of the above basic defects whose interaction with the others is extremely small.

Pure CeO_2 possesses the fluorite structure whereas ZrO_2 has a tetragonal crystal structure at very low dopant concentrations. Then, it is possible in doped CeO_2 to study the defect properties in the fluorite structure systematically over wide range of dopant concentration including at very low dopant concentrations.

The crystal structure of doped CeO_2 is a fluorite type, where Ce^{4+} ions are partly replaced by the dopant cations at random. O^{2-} vacancies are introduced in the O^{2-} ion sublattices to compensate the effective negative charge of the dopant cations. Therefore, the doped CeO_2 loses generally the translational symmetry of the crystal, leading to the destruction of the wave vector $k=0$ selection rule for Raman scattering. Consequently, phonons at all parts in the Brillouin zone will contribute to the optical spectra. It is known that we can get the information about the defect space such as the symmetry and the volume analyzing the defect-induced Raman spectra.

The first-order Raman scattering of pure CeO_2 has been reported by Keramidas and White.[1] The second-order Raman scattering study in CeO_2 was firstly done by Kourouklis, Jayaraman, and Espinosa[2] who tentatively assigned the peaks using pressure-induced spectra from unoriented crystals in a diamond-anvil cell. Recently, Weber, Hass, and McBride[3] measured the polarized Raman-scattering spectra from oriented single crystals of CeO_2 and the second-order Raman features are analyzed on the basis of selection rule. But they did not measure the temperature dependence of the Raman spectra and the phonon-dispersion curves used by them do not completely coincide with the phonon-dispersion curves obtained from the neutron inelastic-scattering measurements.[4] Within the knowledge of the authors, there has been no measurement of the defect-induced Raman spectra of doped CeO_2.

In this study, temperature- and dopant-type dependencies of the Raman-scattering spectra for doped CeO_2 are measured. The polarized Raman spectra are also measured. To understand the defect-induced Raman spectra, it is necessary to know the information about the phonon-dispersion curves over the whole Brillouin zone.

To our knowledge, there are three calculations of the phonon-dispersion curves in CeO_2. In 1982, Sato and Tateyama[5] calculated the phonon-dispersion curves employing a rigid-ion model using the value of $\omega_{LO}=750.3$ cm^{-1} which was quite different from the presently accepted experimental value of $\omega_{LO}=595$ cm^{-1}.[6,7] Furthermore, they assumed the value of elastic constant components being the same as those of ThO_2, which are found to be extremely different from those of CeO_2 determined from our Brillouin-scattering measurements.

In 1993, Weber, Hass, and McBride[3] calculated the phonon-dispersion curves in CeO_2 also employing a rigid-ion model. In the calculation, they used the value of elastic constant components determined from their Raman data and the bulk modulus value.

On the other hand, Clausen *et al.*[4] have already measured the phonon-dispersion relations of CeO_2 using inelastic neutron-scattering measurements in 1987. Since

0163-1829/94/50(18)/13297(11)/$06.00

the data have been measured only below 500 cm^{-1}, they assumed in their phonon dispersion curves calculated employing a shell model the value of $\omega_{LO}=657$ cm^{-1}, which is extremely different from the presently accepted ω_{LO} value of 595 cm^{-1}.

Therefore, we calculated the phonon-dispersion curves in CeO_2 with more reliable parameters for rigid-ion model in this study. The experimental results are compared with frequency distributions of Raman-active modes in the Brillouin zone estimated from the imaginary part of the projection of the phonon displacement-displacement Green's functions of CeO_2 crystal onto several defect spaces. The Brillouin spectra of CeO_2 are measured to calculate the precise phonon-dispersion curves. On the basis of the results of these analyses, the dependencies of type and concentration of the defect space on dopant concentration in doped CeO_2 are discussed.

II. EXPERIMENTAL PROCEDURES

The following transparent samples were grown by xenon-arc image furnace in our laboratory and used for Raman-scattering measurements:

(1) a polycrystalline sample of CeO_2, which was made from CeO_2 powders with 99.999% purity;

(2) oriented single crystals of $(1-x)CeO_2$-$xYO_{1.5}$ $(x=0.02, 0.09, 0.18)$, whose dopant concentrations were calibrated by using an x-ray fluorescence analysis;

(3) polycrystalline samples of $(1-x)CeO_2$-$xYO_{1.5}$ $(x=0.04)$ and $(1-x)CeO_2$-$xLaO_{1.5}$ $(x=0.04)$ and $(1-x)CeO_2$-$xZrO_2$ $(x=0.04)$. The dopant concentrations of these samples are nominal.

By using these transparent samples, grain-boundary effects of samples on the Raman spectra can be excluded and the intensity of stray light scattered by the samples is drastically reduced compared with ceramic samples.

The crystals were cut into a rectangular shape. The single crystals were cut into a shape with (100) faces and one (110) face.

In Brillouin-scattering measurements, we use an oriented single crystal of CeO_2 grown by using a flux of $PbO+PbF_2+B_2O_3$.[8]

All samples are polished to give optical surface. The orientation of the single crystals was determined by Laue back-reflection x-ray analysis.

The Raman spectra were excited by 4880-Å line of 2W NEC Ar^+-ion laser and were analyzed with a double-grating monochromator (Nihon Bunkou CT-1000D) equipped with a photon counting system. The wave number is accurate within 2 cm^{-1}. All Raman spectra were taken in a right-angle scattering geometry.

The Brillouin spectra in the right-angle scattering geometry were measured using a tandem Fabry-Perot interferometer with a grating monochromator served as a band-pass filter which gives a single frequency avoiding the stray light from interference of different orders.[9] The resolution is 0.04 cm^{-1}. In the backscattering geometry, the spectra were obtained using a piezoelectrically scanned five-pass Fabry-Perot interferometer. The free spectral range is 3.2 cm^{-1} and the spectral resolution is 0.05 cm^{-1}.

III. RESULTS

Figure 1 shows the polarization spectra of Brillouin scattering of CeO_2 for a right-angle geometry. As seen in the figure, there are two Brillouin-scattering lines, transverse acoustic (TA) and longitudinal acoustic (LA). The frequency shift of these scattering lines is 0.67 cm^{-1} (TA) and 1.53 cm^{-1} (LA), respectively. The direction of incident light was taken to be along $[\bar{1}00]$ and that of scattered light to be along [010]. In this geometry, the phonons responsible for the scattering have the propagation direction along [110]. Along this direction, one pure longitudinal phonon and two pure transverse phonons can propagate for cubic crystals. The directions of the atomic motion for the two pure transverse phonons are $[1\bar{1}0]$ and [001].

According to the Brillouin-scattering selection rule for a cubic crystal of the point group O_h,[10] the Brillouin-scattering lines due to the transverse phonon with the direction of atomic motion along [001] can be observed in the HV, i.e., horizontal (H) incident polarization and vertical (V) scattered polarization with respect to the scattering plane, and VH (vertical incident, horizontal scattered) polarizations. The Brillouin-scattering lines disappear in the HH and VV polarizations. The Brillouin-scattering lines due to the transverse phonon with the direction of atomic motion along $[1\bar{1}0]$ cannot be observed in any polarization for this scattering geometry. Moreover, the Brillouin-scattering lines due to the longitudinal phonon can be observed in the HH and VV polarizations while they disappear in the HV and VH polarizations according to the selection rule.

Comparing the observed polarization features with the selection rule mentioned above, the Brillouin-scattering line with frequency shift 0.67 cm^{-1} is identified to that due to the transverse-acoustic phonon (TA) and the one with frequency shift 1.53 cm^{-1} to that due to the longitudinal-acoustic phonon (LA).

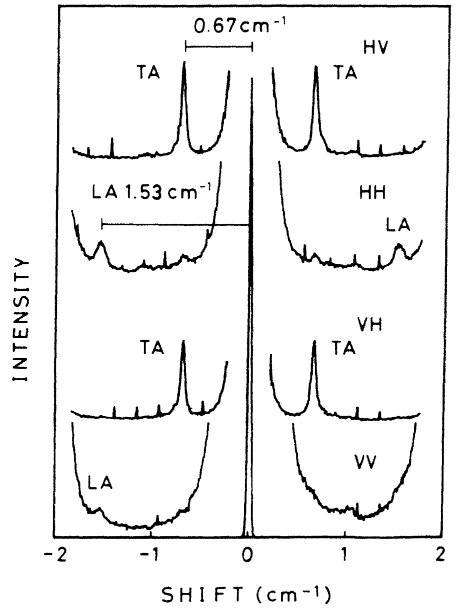

FIG. 1. Polarization dependence of Brillouin-scattering spectra taken in the right-angle geometry.

In a cubic crystal of CeO_2, we can estimate the sound velocity V_s for each phonon mode from the frequency shift f of the Brillouin-scattering lines through following equation:[10]

$$V_s = \frac{f\lambda_0}{2n\sin(\theta/2)} , \tag{1}$$

where λ_0 is the wavelength of the incident light, n is the refractive index of CeO_2, and θ is the scattering angle.

For the [110] propagating transverse phonon mode, the sound velocity V_{s1} is calculated as 2.89×10^5 (cm/s) using Eq. (1). Then, the component of elastic constant C_{44} can be calculated as 6.0×10^{11} (dyn/cm^2) using the following equation:

$$\rho V_{s1}^2 = C_{44} , \tag{2}$$

where ρ is the crystal density of CeO_2.

For the [110] propagating longitudinal phonon mode, the sound velocity V_{s2} is calculated as 6.60×10^5 (cm/s). There is a relation between the components of elastic constant and the sound velocity for this phonon mode as follows:

$$\rho V_{s2}^2 = (C_{11}+C_{12}+2C_{44})/2 . \tag{3}$$

Figure 2 shows the Brillouin-scattering spectra for a backscattering geometry. Two Brillouin-scattering lines, TA and LA are seen in this figure. The direction of the incident light was taken to be along $[\bar{1}00]$ and that of the scattered light to be along [100]. In this scattering geometry, the phonons responsible for the scattering have the propagation direction along [100]. Along this direction, the degenerate pure transverse phonon mode and the pure longitudinal phonon mode can propagate for cubic crystals. The directions of the atomic motion are [010] and [001] for the degenerate pure transverse phonon mode.

For the [100] propagating transverse phonon mode, we can estimate the component of elastic constant C_{44} from the following equation:

$$\rho V_{s3}^2 = C_{44} , \tag{4}$$

where V_{s3} is the sound velocity of this phonon mode in the backscattering geometry. Using the sound velocity V_{s4} of the [100] propagating longitudinal phonon mode, on the other hand, we can estimate the component of elastic constant C_{11} from the following equation:

$$\rho V_{s4}^2 = C_{11} . \tag{5}$$

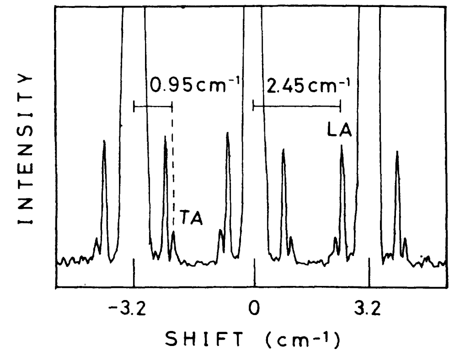

FIG. 2. Brillouin-scattering spectra taken in the backscattering geometry.

Since the spectra in Fig. 2 are not polarized, it is difficult to assign the Brillouin-scattering lines to the above two phonon modes using the polarization selection rule. Then, we assigned the Brillouin-scattering lines in Fig. 2 to the phonon modes as follows:

First, we assume the frequency shift of the TA line to be 0.95 cm^{-1} as shown in Fig. 2 and the phonon mode responsible for this Brillouin line to be the [100] propagating transverse phonon. Then, the value of elastic component C_{44} can be evaluated to be 6.0×10^{11} (dyn/cm^2) from the frequency shift using Eqs. (1) and (4). Since this value coincides with that of the C_{44} value evaluated from the frequency shift of [110] propagating transverse phonon mode shown in Fig. 1 using Eqs. (1) and (2), the TA line in Fig. 2 is concluded to be attributed to the [100] propagating transverse phonon mode. Then, the LA line in Fig. 2 is concluded to be attributed to the [100] propagating longitudinal phonon mode.

For the [100] propagating longitudinal phonon mode, the calculated value of elastic component C_{11} best coincides with that obtained from the neutron-scattering measurements[4] when we take the frequency shift of the Brillouin lines as 2.45 cm^{-1}. Therefore, we decided that the frequency shift of the LA line is 2.45 cm^{-1} for the [100] propagating longitudinal phonon mode in Fig. 2. The value of elastic component C_{11} is evaluated to be 4.03×10^{12} (dyn/cm^2) from the frequency shift of 2.45 cm^{-1} using Eq. (5). Then, the value of elastic component C_{12} is calculated as 1.05×10^{12} (dyn/cm^2) from Eq. (3) using the values of C_{11}, C_{44}, and V_{s2} determined before. The values of elastic components thus obtained are tabulated in Table I.

Figure 3 shows the Raman spectra of pure CeO_2 obtained at 15 K. Only the sharp line at 465 cm^{-1} is observed. On the other hand, the Raman spectra for the sample of $(1-x)CeO_2$-$xYO_{1.5}$ $(x=0.18)$ obtained at 15 K exhibit several continuously spread bands, as seen in Fig. 4(b). For such broad Raman bands, two origins are possible. One is the defect-induced first-order Raman effect and the other is the second-order Raman effect by two-phonon process. It is well known that the intensity of Raman band varies with temperatures as $(n+1)$ for first-order Raman effect and as $(n+1)(n'+1)$ or $n(n'+1)$ for second-order Raman effect, where $n=[\exp(h\nu/kT)-1]^{-1}$, $h\nu$ is the phonon energy and k the Boltzmann constant. Thus, the temperature dependence of Raman spectra are measured in order to confirm whether the broad spectra are first order or second order.

Figure 4(a) shows the Raman spectra for the sample of $(1-x)CeO_2$-$xYO_{1.5}$ $(x=0.18)$ reduced by using the temperature factor $(n+1)$ from 300 to 15 K. In Figs. 4(a) and 4(b), it is seen that the frequency dependence of the reduced spectra shows a good agreement with the one observed at low temperature. When the temperature factor for second-order Raman effect is used, the considerable

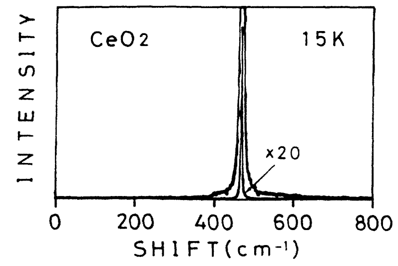

FIG. 3. Raman-scattering spectra in pure CeO_2.

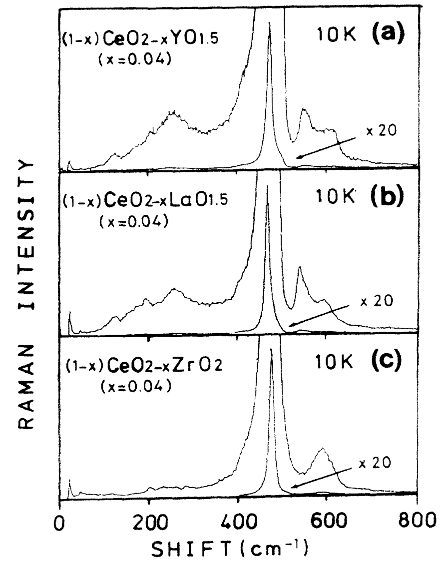

FIG. 5. Dopant-type dependence of Raman-scattering spectra for doped CeO_2. (a) The spectra for Y^{3+}-doped CeO_2. (b) The spectra for La^{3+}-doped CeO_2. (c) The spectra for Zr^{4+}-doped CeO_2.

discrepancy between the spectra at low temperature and the reduced ones exists. Therefore, it is concluded that the observed Raman spectra for the sample of $(1-x)CeO_2$-$xYO_{1.5}$ $(x=0.18)$ are caused by first-order Raman effect which may be attributed to defect spaces involved in the sample.

To see what types of defect space contribute to the Raman bands, we varied the dopant kind in doped CeO_2 and investigated the change of Raman spectra by dopant kind. Figures 5(a), 5(b), and 5(c) show the Raman spectra of doped CeO_2 whose dopant cation is Y^{3+}, La^{3+}, and Zr^{4+}, respectively. In these figures, the spectra of Y^{3+}-doped CeO_2 and that of La^{3+}-doped CeO_2 are almost the same in structure but the spectra of Zr^{4+}-doped CeO_2 are not similar to those of the former two. The most striking characteristic is that the Raman bands at the frequency region below 400 cm^{-1} and the Raman peak around 540 cm^{-1} have almost disappeared for Zr^{4+}-doped CeO_2.

In both of Y^{3+}-doped CeO_2 and La^{3+}-doped CeO_2, the O^{2-}vacancies are introduced as defects as well as dopant cations to keep charge neutrality. In the case of Zr^{4+}-doped CeO_2, on the other hand, only the dopant cations are introduced as defects without O^{2-} vacancies. Since the Raman peak around 600 cm^{-1} is observed in all Raman spectra in Figs. 5(a), 5(b), and 5(c), the defect spaces including a dopant cation without any O^{2-} vacancy are considered to contribute to the Raman peak. On the other hand, the broad Raman bands below 400 cm^{-1} and the Raman peak around 540 cm^{-1} are attributed to the defect space which includes an O^{2-} vacancy because they are only observed in Figs. 5(a) and 5(b).

As the crystal structure of doped CeO_2 used in this study is fluorite-type which belongs to the space group O_h^5, the Raman tensor transforms as irreducible representation $A_{1g}+E_g+T_{2g}$. Then, the Raman spectra can be decomposed into the spectra belonging to each Raman-active irreducible component by the polarization mea-

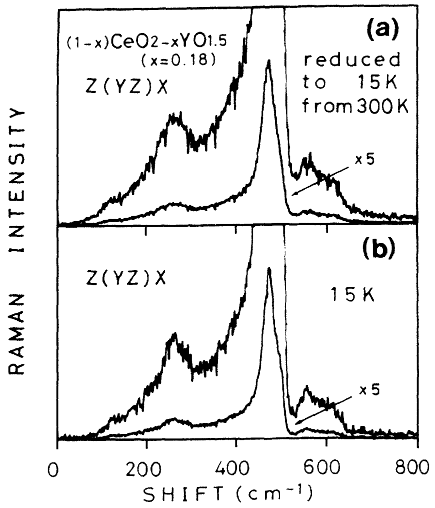

FIG. 4. Raman-scattering spectra for doped CeO_2. (a) The spectra reduced from 300 to 15 K. (b) The spectra taken at 15 K.

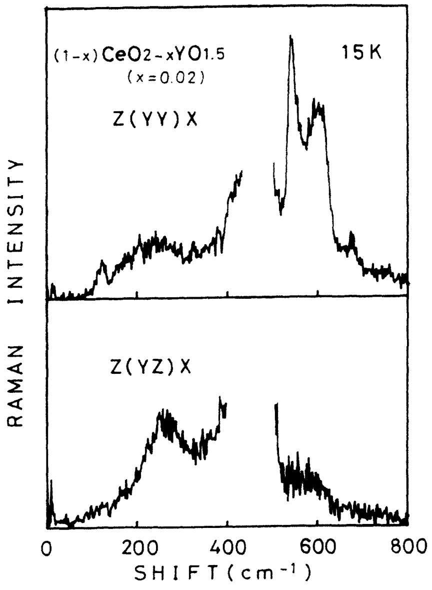

FIG. 6. Polarized Raman-scattering spectra for doped CeO_2 $(x=0.02)$ taken at 15 K.

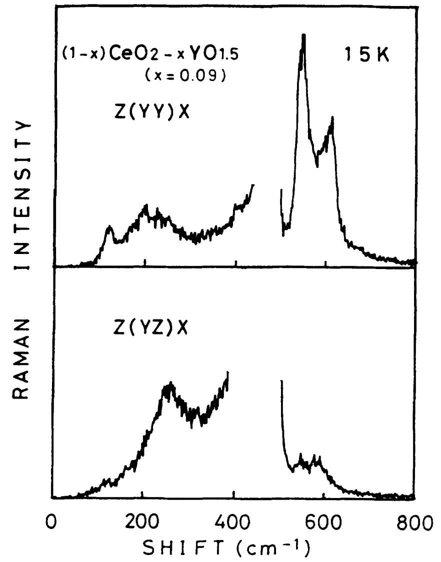

FIG. 7. Polarized Raman-scattering spectra for doped CeO_2 ($x=0.09$) taken at 15 K.

surements. Using the orthogonal Cartesian coordinates system X-Y-Z defined as $X=[100]$, $Y=[010]$, $Z=[001]$, the spectra belonging to T_{2g} symmetry will be measured by using the polarization $Z(YZ)X$ and the spectra belonging to $A_{1g}+E_g$ by the polarization $Z(YY)X$.

Figure 6 shows the polarized defect-induced Raman spectra of $(1-x)CeO_2$-$xYO_{1.5}$ ($x=0.02$) obtained at 15 K. As shown in this figure, the spectra show a clear polarization dependence. Figures 7 and 8 also show the polarized defect-induced Raman spectra of $(1-x)CeO_2$-$xYO_{1.5}$ ($x=0.09$) and $(1-x)CeO_2$-$YO_{1.5}$ ($x=0.18$), respectively.

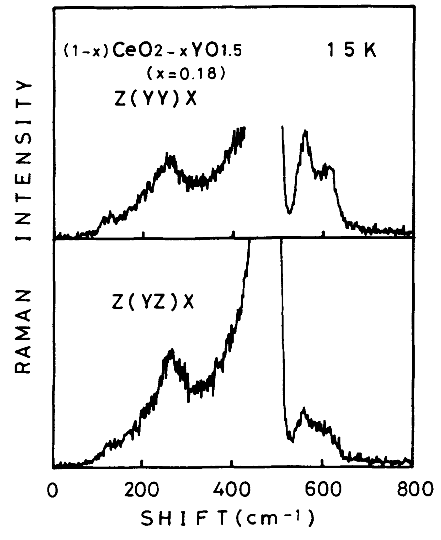

FIG. 8. Polarized Raman-scattering spectra for doped CeO_2 ($x=0.18$) taken at 15 K.

IV. DISCUSSION

A. Lattice dynamics of CeO_2

We calculated the phonon-dispersion curves in CeO_2 employing a rigid-ion model using the values of the elastic constant components determined using our Brillouin-scattering measurements and ω_{LO} value which agree with the experimentally accepted one. The detail descriptions of the rigid-ion model are given in other papers.[11,12]

After the application of symmetries for CeO_2, the short-range force-constant matrix Φ for the nearest-neighbor cation-anion interaction is given as follows:

$$\Phi(\mathrm{Ca-O})=\begin{vmatrix}\alpha_1 & \beta_1 & \beta_1\\ \beta_1 & \alpha_1 & \beta_1\\ \beta_1 & \beta_1 & \alpha_1\end{vmatrix} . \tag{6}$$

For the second-neighbor cation-cation interaction, the force-constant matrix is

$$\Phi(\mathrm{Ca-Ca})=\begin{vmatrix}\alpha_2 & 0 & 0\\ 0 & \beta_2 & \gamma_2\\ 0 & \gamma_2 & \beta_2\end{vmatrix} , \tag{7}$$

and for the second-neighbor anion-anion interaction, the force-constant matrix is

$$\Phi(\mathrm{O-O})=\begin{vmatrix}\beta_3 & 0 & 0\\ 0 & \beta_3 & 0\\ 0 & 0 & \alpha_3\end{vmatrix} . \tag{8}$$

Assuming the force constant α_2 and β_3 to be zero according to Ganesan and Srinivasan,[12] the number of the unknown parameter for the rigid-ion model is six, namely, α_1, β_1, γ_2, β_2, α_3, and Z which is the effective charge. To evaluate these six parameters, the data given in Table I are used. In this table, the values of elastic constants C_{11}, C_{12}, and C_{44} are those obtained from our Brillouin-scattering measurements described before. The values of ω_{TO} and ω_{LO} are obtained from the infrared reflectivity measurements reported by Ohura.[13] These values are almost the same as the presently accepted experimental values: 595 cm^{-1} for ω_{LO} and 272 cm^{-1} for ω_{TO}.

Using these values, the six unknown rigid ion model parameters are determined. Values of the parameters are given in Table II. Using the values of the parameters in Table II, the phonon-dispersion curves are calculated along three symmetry directions [100], [110], and [111]

TABLE I. Experimental results on CeO_2. C_{11}, C_{12}, C_{44} are the components of elastic constant. ω_R, ω_{TO}, and ω_{LO} are Raman, infrared resonance, and longitudinal optic frequencies, respectively.

C_{11} (10^{12} dyn/cm^2)	C_{12} (10^{12} dyn/cm^2)	C_{44} (10^{12} dyn/cm^2)	ω_R (cm^{-1})	ω_{LO} (cm^{-1})	ω_{TO} (cm^{-1})
4.03	1.05	0.60	465	273	597

TABLE II. Force-constant parameters for the rigid-ion model.

α_1 (10^4 dyn/cm)	β_1 (10^4 dyn/cm)	β_2 (10^4 dyn/cm)	γ_2 (10^4 dyn/cm)	α_3 (10^4 dyn/cm)	Z
3.23	1.18	1.61	−5.04	1.87	0.61

and are presented in Fig. 9.

In contrast with the calculation of Weber, Hass, and McBride,[3] the phonon-dispersion curves we calculated shows that the Δ_2' branch disperses strongly enough to cross the Δ_5 branch which connects to the TO mode at Γ as the data of neutron-scattering measurements.[4] Moreover, also contrary to those of Weber, Hass, and McBride, all the frequencies below 260 cm^{-1} correspond with those of the neutron data fairly well. The correspondence of frequency is excellent especially for the Δ_5 branch which connects to the TA mode at Γ, the Δ_1 branch which connects to the LA mode at Γ, the Λ_1 branch which connects to LA at Γ and the Σ_1 branch which connects to LA at Γ. So, our calculated curves below 500 cm^{-1} fairly agree with the neutron data. We consider that the discrepancies in the phonon-dispersion curves of Weber, Hass, and McBride are mainly due to the uncertainty of the values of elastic constant components used by them in their calculation. Our calculated phonon-dispersion curves above 500 cm^{-1} are also regarded as reasonable.

B. Defect-induced Raman spectra

As seen in Fig. 5, the defect-induced Raman peak around 540 cm^{-1} and below 400 cm^{-1} are attributed to the defect spaces including an O^{2-} vacancy. Then, we will analyze the data assuming that the defect-induced Raman spectra in $(1-x)\mathrm{CeO}_2$-$x\mathrm{YO}_{1.5}$ $(x=0.02)$ are mainly attributed to the defect space including an O^{2-} vacancy.

Figure 10 shows the atomic configuration around the O^{2-} vacancy. As seen in this figure, there are four metal ions in the nearest-neighbor position from an O^{2-} vacancy. In the next-nearest-neighbor positions from the O^{2-} vacancy, there are six O^{2-} ions.

As a first step, we assume that the defect space consists of an O^{2-} vacancy and surrounding four nearest-neighbor metal ions as shown in Fig. 10(a). Hereafter, we will refer to this defect space as an M_4O_v-type complex where O_v is an O^{2-} vacancy. Since this M_4O_v-type com-

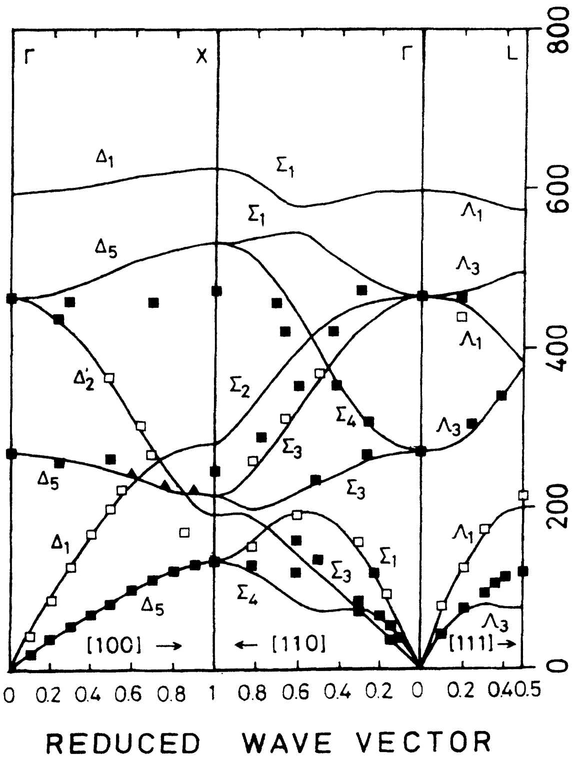

FIG. 9. Phonon-dispersion curves in CeO_2 calculated using the rigid-ion model along the high-symmetry directions for the fluorite structure. Squares and triangles are the neutron inelastic-scattering data obtained by Clausen *et al.* (Ref. 4). Closed (open) squares are predominantly transverse (longitudinal) modes.

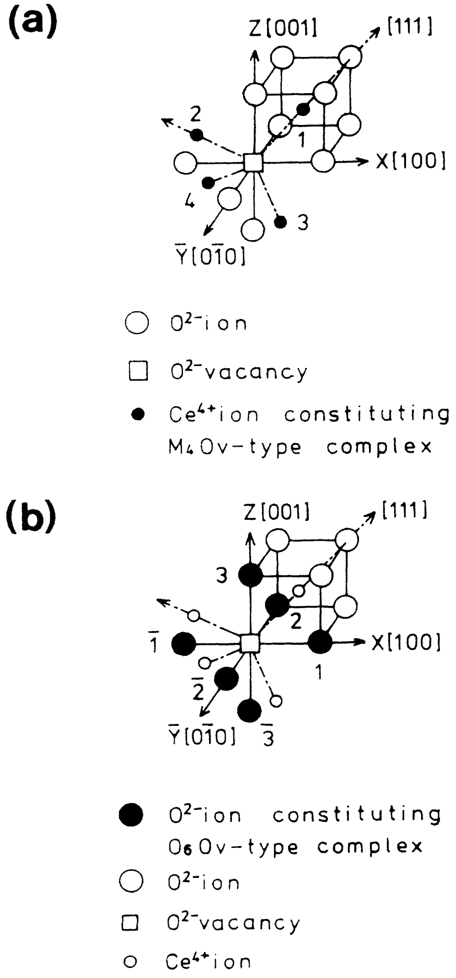

FIG. 10. The defect spaces including an O^{2-} vacancy. (a) M_4O_v-type defect space. (b) O_6O_v-type defect space.

plex has 12 degrees of freedom and possesses T_d symmetry, vibrational normal modes of this M_4O_v-type complex are given by the group operation of point group T_d as follows: $\Gamma = A_1 + E + T_1 + 2T_2$. The unnormalized mode vectors for an M_4O_v-type complex are shown in Table III. In these modes, Raman-active modes are A_1, E, and T_2.

By using phonon displacement-displacement Green's functions $G(\omega+i\varepsilon)$ and taking the imaginary part of the simple projections of $G(\omega+i\varepsilon)$ onto this defect space, we can estimate the defect-induced Raman spectra. According to the theoretical treatment by Lacina and Pershan,[14] the defect-induced Raman spectra are represented by the distribution of frequencies for Raman-active modes given by the following equations:

$$I(\omega, A_1) \propto \mathrm{Im}\langle A_1 | G(\omega+i\varepsilon) | A_1 \rangle \ , \tag{9}$$

$$I(\omega, E) \propto \mathrm{Im}\langle E | G(\omega+i\varepsilon) | E \rangle \ , \tag{10}$$

$$I(\omega, T_2) \propto \mathrm{Im}\langle T_2 | G(\omega+i\varepsilon) | T_2 \rangle \ . \tag{11}$$

Here, $\langle A_1|$, $\langle E|$, and $\langle T_2|$ are the normalized Raman-active mode vectors in an M_4O_v-type complex.

In the calculation, the $G(\omega+i\varepsilon)$ for the perturbed crystal by the introduction of defects is assumed to be the phonon Green's functions $G_0(\omega+i\varepsilon)$ for the perfect crystal as the first approximation. The calculated frequency distributions for each symmetry are shown by histograms in Fig. 11.

According to the Raman-scattering tensor for T_d symmetry, the Raman spectra belonging to T_2 symmetry will be measured using the polarization $Z(XY)X$, and the spectra belonging to A_1+E using the polarization $Z(YY)X$. When a new coordinate system $X'=X-Y$, $Y'=X+Y$, and $Z'=Z$ is used, the $Z'(Y'X')Y'$ measurement gives the spectra belonging only to E symmetry. Therefore, these three independent measurements suffice to separate irreducible components of Raman spectra. Broken curves in Fig. 11 are thus obtained irreducible components from the observed polarization Raman spectra for $(1-x)CeO_2$-$xYO_{1.5}$ $(x=0.02)$.

For all irreducible components, as seen in the figure, the calculated results only appear in the low-frequency region compared with the observed spectra. This is considered that the projection of high-frequency components of $G(\omega+i\varepsilon)$ in Eqs. (9)–(11) due to the vibration of O^{2-} ion in the Brillouin zone are lost because the used defect space (M_4O_v-type complex) consists of only metal ions with heavy mass neglecting O^{2-} ions with light mass. Consequently, it is insufficient to consider the M_4O_v-type complex in order to elucidate the observed Raman spectra for $(1-x)CeO_2$-$xYO_{1.5}$ $(x=0.02)$. Thus, we will consider the effect of O^{2-} ions in the defect space on the displacement-displacement phonon Green's functions $G(\omega+i\varepsilon)$ in the following discussion.

TABLE III. Unnormalized mode vectors for an M_4O_v-type complex given by the decomposition using group analysis.

	A_1	E		T_1			$T_2(1)$			$T_2(2)$		
	1	−2	0	0	1	1	1	0	0	−2	0	0
1	1	1	1	1	0	−1	0	1	0	−1	3	0
	1	1	−1	−1	−1	0	0	0	1	−1	1	−1
	−1	2	0	0	1	−1	1	0	0	0	−2	−1
2	−1	−1	−1	1	0	1	0	1	0	1	1	−1
	1	1	−1	1	1	0	0	0	1	1	−1	1
	1	−2	0	0	−1	−1	1	0	0	2	0	0
3	−1	−1	−1	−1	0	−1	0	1	0	−1	−1	1
	−1	−1	1	1	−1	0	0	0	1	−1	−3	0
	−1	2	0	0	−1	1	1	0	0	0	2	1
4	1	1	1	−1	0	1	0	1	0	1	−3	0
	−1	−1	1	−1	1	0	0	0	1	1	3	0

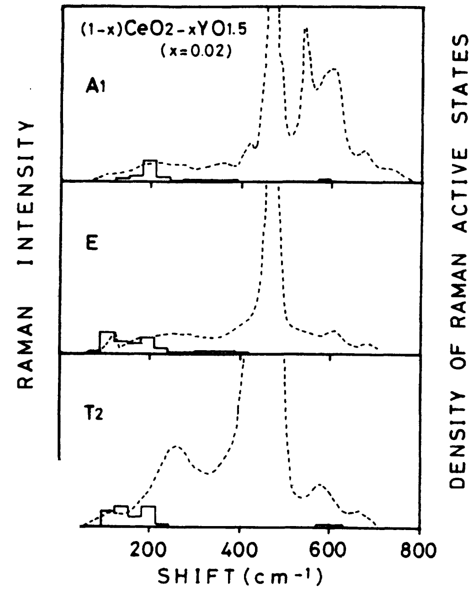

FIG. 11. The frequency distributions of the defect-induced Raman spectra which are the imaginary part of the A_1, E, T_2 symmetry Green's functions calculated using mode vectors of the M_4O_v-type defect space. Broken curves are the irreducible components obtained using the observed polarized Raman spectra.

Then, we will assume that the defect space consists of an O^{2-} vacancy and surrounding six-next-nearest-neighbor O^{2-} ions, ignoring surrounding four metal ions as shown in Fig. 10(b). Hereafter, we will refer to this defect space as an O_6O_v-type complex. Since the O_6O_v-type complex has 18 degrees of freedom and possesses O_h symmetry, vibrational normal modes of this O_6O_v-type complex are given by the group operation of point group O_h as follows: $\Gamma = A_{1g} + E_g + T_{1g} + T_{2g} + 2T_{1u} + T_{2u}$. The unnormalized mode vectors for an O_6O_v-type complex are shown in Table IV. In these modes, Raman-active modes are A_{1g}, E_g, and T_{2g}.

As described before, the Raman spectra induced by this defect space are represented by the distribution of frequencies for Raman-active modes given by the following equations:

$$I(\omega, A_{1g}) \propto \mathrm{Im}\langle A_{1g} | G(\omega+i\varepsilon) | A_{1g} \rangle \ , \tag{12}$$

$$I(\omega, E_g) \propto \mathrm{Im}\langle E_g | G(\omega+i\varepsilon) | E_g \rangle \ , \tag{13}$$

$$I(\omega, T_{2g}) \propto \mathrm{Im}\langle T_{2g} | G(\omega+i\varepsilon) | T_{2g} \rangle \ . \tag{14}$$

TABLE IV. Unnormalized mode vectors for an O_6O_v-type complex given by the decomposition using group analysis.

	A_{1g}	E_g		T_{1g}			T_{2g}			$T_{1u}(1)$			$T_{1u}(2)$			T_{2u}		
	1	−2	0	0	0	0	0	0	0	1	0	0	−1	0	0	0	0	0
1	0	0	0	0	0	1	0	0	1	0	1	0	0	1	0	0	1	0
	0	0	0	0	−1	0	0	1	0	0	0	1	0	0	1	0	0	−1
	0	0	0	0	0	−1	0	0	1	1	0	0	1	0	0	−1	0	0
2	1	1	−1	0	0	0	0	0	0	0	1	0	0	−1	0	0	0	0
	0	0	0	1	0	0	1	0	0	0	0	1	0	0	1	0	0	1
	0	0	0	0	1	0	0	1	0	1	0	0	1	0	0	1	0	0
3	0	0	0	−1	0	0	1	0	0	0	1	0	0	1	0	0	−1	0
	1	1	1	0	0	0	0	0	0	0	0	1	0	0	−1	0	0	0
	−1	2	0	0	0	0	0	0	0	1	0	0	−1	0	0	0	0	0
$\bar{1}$	0	0	0	0	0	−1	0	0	−1	0	1	0	0	1	0	0	1	0
	0	0	0	0	1	0	0	−1	0	0	0	1	0	0	1	0	0	−1
	0	0	0	0	0	1	0	0	−1	1	0	0	1	0	0	−1	0	0
$\bar{2}$	−1	−1	1	0	0	0	0	0	0	0	1	0	0	−1	0	0	0	0
	0	0	0	−1	0	0	−1	0	0	0	0	1	0	0	1	0	0	1
	0	0	0	0	−1	0	0	−1	0	1	0	0	1	0	0	1	0	0
$\bar{3}$	0	0	0	1	0	0	−1	0	0	0	1	0	0	1	0	0	−1	0
	−1	−1	−1	0	0	0	0	0	0	0	0	1	0	0	−1	0	0	0

Here, $\langle A_{1g}|$, $\langle E_g|$, and $\langle T_{2g}|$ are the normalized Raman-active mode vectors in an O_6O_v-type complex. In the calculation, we also use the phonon Green's functions $G_0(\omega+i\varepsilon)$ for the perfect crystal. The calculated frequency distribution for each symmetry is shown by the histograms in Fig. 12.

According to the Raman-scattering tensors for O_h symmetry, the Raman spectra belonging to T_{2g} symmetry will be measured using the polarization $Z(XY)X$, the spectra belonging to $A_{1g}+E_g$ using the polarization $Z(YY)X$, and the spectra belonging to E_g using the polarization $Z'(Y'X')Y'$. Therefore, we can separate irreducible components of Raman spectra using these three polarization measurements as the same manner described before.

Broken curves in Fig. 12 are irreducible components obtained from the observed polarization Raman spectra for $(1-x)\mathrm{CeO_2}$-$x\mathrm{YO_{1.5}}$ $(x=0.02)$. Except for the E_g component of the Raman spectra, the calculated results appear in all the frequency region where the experimental Raman spectra are observed. In the calculated frequency distribution with A_{1g} symmetry, two distinct peaks appear at around 200 and 600 cm^{-1} in addition to a broad band extended from 100 to 650 cm^{-1}. In this figure, the calculated frequency distribution seems to reproduce the observed Raman spectra for A_{1g} symmetry though there is a discrepancy in peak frequency between 600 cm^{-1} in the calculated distribution and 540 cm^{-1} in the observed spectra. For T_{2g} symmetry, it is seen that the calculated frequency distribution is considerably similar to the observed Raman spectra except for the relative intensity of the peak around 600 cm^{-1}.

On the contrary, the calculated frequency distribution does not sufficiently reproduce the observed Raman spectra for E_g symmetry. Especially, the height of the calculated histograms below 250 cm^{-1} is extremely small compared with that of observed spectra. Then, we took the linear combination of the calculated frequency distributions from the M_4O_v-type complex and from the O_6O_v-type complex in order to approximate the frequency distributions obtained from the observed Raman spectra more precisely.

The calculated frequency distributions obtained from the linear combination are shown by the histograms in Fig. 13. In this figure, broken curves are the spectra ob-

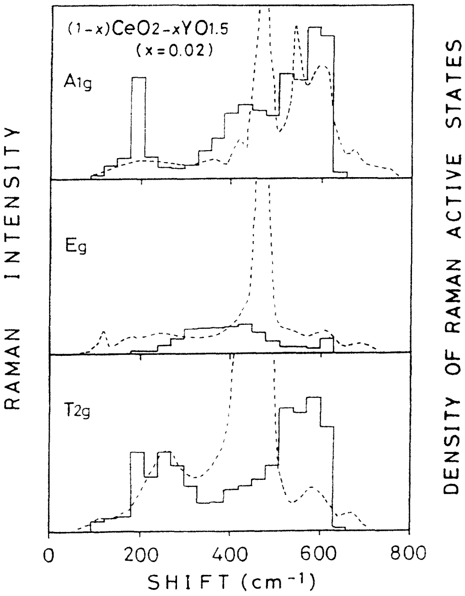

FIG. 12. The frequency distributions of the defect-induced Raman spectra which are the imaginary part of the A_{1g}, E_g, T_{2g} symmetry Green's functions calculated using mode vectors of the O_6O_v-type defect space. Broken curves are the irreducible components obtained using the observed polarized Raman spectra.

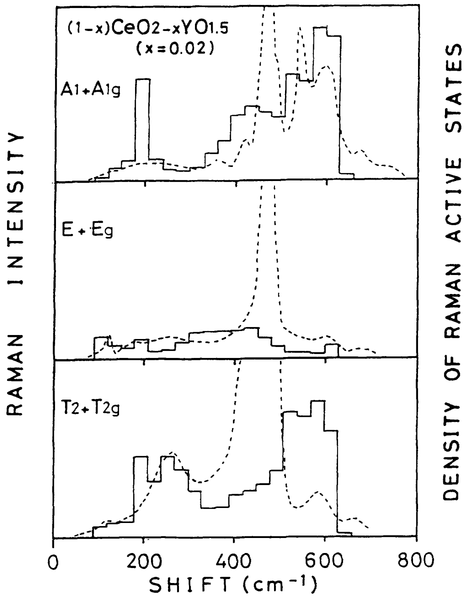

FIG. 13. The frequency distributions of the defect-induced Raman spectra which result from the linear combination of those from the M_4O_v-type and O_6O_v-type defect spaces. Broken curves are the irreducible components obtained using the observed polarized Raman spectra.

tained from the observed polarization Raman spectra. This time, not only for the symmetries of A_1+A_{1g} and of T_2+T_{2g} but also for the symmetry of $E+E_g$, the calculated frequency distributions well reproduce the observed Raman spectra.

In this analysis, we found that the frequency distributions from the M_4O_v-type complex only appear in the low-frequency region (below 250 cm^{-1}), while those from the O_6O_v-type complex appear in almost the whole frequency region except for E_g components. We consider this difference of the frequency distribution is due to the large difference of mass between Ce^{4+} ion and O^{2-} ion.

We also consider that this large mass difference between Ce^{4+} ion and O^{2-} ion explains the good correspondence between the observed Raman spectra and the linear combination results of the calculated frequency distributions from the M_4O_v-type complex and the O_6O_v-type complex. In other words, large mass difference between Ce^{4+} ion and O^{2-} ion may assure that the vibration modes of M_4O_v-type complex and those of O_6O_v-type complex are independent of each other.

Certainly, taking account of the defect space consisting of the four metal ions and of the six O^{2-} ions surrounding an O^{2-} vacancy will result in a better correspondence to the observed Raman spectra. In a future publication, we will show the improved calculation results in this manner.

C. Dependencies of type and concentration of defect space on dopant concentration

As shown in Figs. 6–8 with (*YY*) polarization, the peak intensity around 600 cm^{-1} decreases with increasing x relative to the maximum intensity in the region from 200 to 260 cm^{-1}. Two possibilities are considered as the reason for this decrease. One is that the phonon-dispersion curves of $(1-x)CeO_2$-$xYO_{1.5}$ change with increasing x. The other is that the type and concentration of the defect space vary with increasing x.

Since the peak frequency around 260 cm^{-1} with (*YZ*) polarization and those around 120 and 600 cm^{-1} with (*YY*) polarization do not change with increasing x in Figs. 6, 7, and 8, the phonon-dispersion curves of $(1-x)CeO_2$-$xYO_{1.5}$ are considered to be unchanged with increasing x in the region below $x=0.18$. Therefore, the decrease of the peak intensity around 600 cm^{-1} with increasing x is considered to be attributed to the change of the type and concentration of the defect space.

As described before, the Raman peak around 600 cm^{-1} with (*YY*) polarization is attributed to the defect space including a dopant cation. This defect space is shown in Fig. 14(a) and has O_h symmetry without having any O^{2-} vacancy. Hereafter, we will refer to this defect space as MO_8-type complex. Then, the decrease of the Raman peak intensity around 600 cm^{-1} with (*YY*) polarization with increasing x suggests that the concentration of MO_8-type complex relative to those of the other type of defect space decreases with increasing x. Anderson and Nowick[15] suggested the existence of the defect space shown in Fig. 14(b) for $(1-x)CeO_2$-$xYO_{1.5}$ $(x=0.04)$ from anelastic relaxation. The existence of the defect space shown in Fig. 14(d) is also suggested in $(1-x)CeO_2$-$xYO_{1.5}$ $(x=0.12)$ from neutron inelastic-scattering measurement.[16] The defect space shown in Fig. 14(c) is also considered to exist below $x=0.18$ by analogy.

In the defect spaces (b)–(d) shown in Fig. 14, (b) and (c) can be decomposed to the space which does not include any O^{2-} vacancy (the region in the circle drawn) and the space which includes an O^{2-} vacancy (the region out of the circle drawn). Since the former space consists of a dopant cation and of the eight nearest-neighbor O^{2-} ions, it resembles the MO_8-type complex. Strictly speaking, however, the space differs from the MO_8-type complex since the space no longer has O_h symmetry due to the effect of the neighboring O^{2-} vacancy. The lack of O^{2-} ions at an O^{2-} ion site changes the interatomic forces between the ions near the site. This changes the equilibrium positions of the ions near the O^{2-} vacancy, leading to the symmetry change of the above space from O_h symmetry. For this reason, the vibrational state of the spaces in the circle shown in (b) and (c) is thought to be different from that of the MO_8-type complex.

For the defect space (d) shown in Fig. 14, it cannot even be decomposed to the space which consists of a dopant cation and of the eight nearest-neighbor O^{2-} ions and the space which includes an O^{2-} vacancy as the former two defect spaces can be done. Then, the vibrational state of this defect space (d) is also different from that of the MO_8-type complex (a). Therefore, the decrease of the Raman peak intensity around 600 cm^{-1} for (*YY*) polarization with increasing x can be explained by the fact that the concentrations of the defect spaces (b)–(d) shown in Fig. 14, relative to that of the MO_8-type complex (a), increase with increasing x.

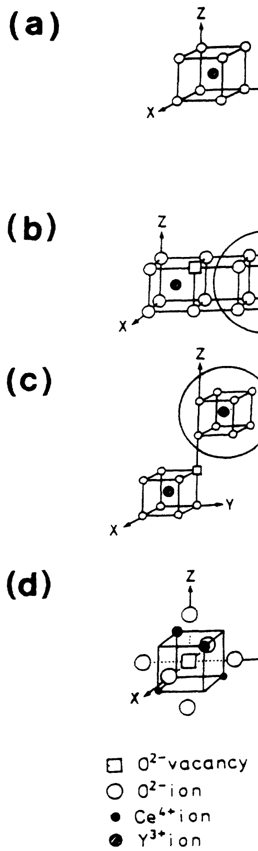

FIG. 14. Four kinds of defect spaces expected to exist in $(1-x)CeO_2$-$xYO_{1.5}$.

It is noteworthy that there are some characteristics of spectral change with increasing x in addition to the change of Raman spectra described before. As seen in Figs. 6, 7, and 8, there is a clear Raman peak around 260 cm^{-1} in the Raman spectra with (YY) polarization of $(1-x)CeO_2$-$xYO_{1.5}$ $(x=0.18)$, while there is not a clear peak around 260 cm^{-1} in the Raman spectra with (YY) polarization of $x=0.02$ and $x=0.09$. Moreover, a peak appears around 540 cm^{-1} in the Raman spectra with (YY) polarization of $x=0.02$ and $x=0.09$, while this peak shifts to around 560 cm^{-1} in the spectra of $x=0.18$. These characteristics of spectral change suggest that comparatively large change of the vibrational state of defect space takes place between $x=0.09$ and $x=0.18$.

A relatively large change of the vibrational state from that of MO_8-type complex is expected for the defect space (d) shown in Fig. 14 rather than for the defect spaces (b) and (c) shown in Fig. 14. As described before, the defect spaces (b) and (c) shown in Fig. 14 have the space which includes a dopant cation and eight nearest-neighbor O^{2-} ions. Although an O^{2-} vacancy is sited near the spaces, the symmetry of the spaces is considered to be not so much different from O_h symmetry. On the other hand, the defect space (d) shown in Fig. 14 no longer has such space. So, the symmetry of the defect space is far from O_h symmetry. Then, the extent of the difference of the vibrational state of the former two defect spaces from that of the MO_8-type complex are considered to be less than that of the latter defect space. Therefore, the comparatively large change in the Raman spectra of $x=0.18$ suggests that the large concentration increase of the defect space (d) shown in Fig. 14 relative to those of the defect spaces (b) and (c) shown in Fig. 14 occurs between $x=0.09$ and $x=0.18$.

V. CONCLUSION

In summary, we have obtained polarized defect-induced Raman spectra from oriented single crystals of yttria-doped CeO_2. In order to assign the spectra due to the defect space, we examined the dopant-type dependence of the defect-induced Raman spectra of doped CeO_2 and calculated the defect-induced Raman-active modes in the whole Brillouin zone which are estimated from the imaginary part of the simple projection of the phonon displacement-displacement Green's functions onto several defect spaces.

From this analysis, the polarization characteristics and the frequency dependence of Raman spectra in yttria-doped CeO_2 are well explained by the linear combination of the frequency distribution from the defect space consisting of the four nearest-neighbor metal ions and from that consisting of the six next-nearest-neighbor O^{2-} ions surrounding an O^{2-} vacancy.

In order to calculate the phonon-dispersion curves, Brillouin-scattering spectra are also measured. The dependencies of type and concentration of defect space on dopant concentration in doped CeO_2 suggest that the concentration of the MO_8-type complex decreases in $(1-x)CeO_2$-$xYO_{1.5}$ with increasing x and that the comparatively large increase of the concentration of the defect space which includes an O^{2-} vacancy and the nearest-neighbor two dopant cations takes place between $x=0.09$ and $x=0.18$.

ACKNOWLEDGMENTS

The authors are indebted to Dr. S. Shin, Dr. H. Arashi, Dr. H. Yugami, and Dr. T. Suemoto for useful discussions. This work was partially supported by a Grant-in-Aid for Scientific Research from the Ministry of Education of Japan.

---

*Present address: Fujitsu Laboratories, Ltd., 10-1 Morinosato-Wakamiya, Atsugi-shi, Kanagawa-ken 243-01, Japan.

[1] V. G. Keramidas and W. B. White, J. Chem. Phys. **59**, 1561 (1973).
[2] G. A. Kourouklis, A. Jayaraman, and G. P. Espinosa, Phys. Rev. B **37**, 4250 (1988).
[3] W. H. Weber, K. C. Hass, and J. R. McBride, Phys. Rev. B **48**, 178 (1993).
[4] K. Clausen, W. Hayes, J. E. Macdonald, R. Osborn, P. G. Schnabel, M. T. Hutchings, and A. Magerl, J. Chem. Soc.

Faraday Trans. 2 **83**, 1109 (1987).

[5] T. Sato and S. Tateyama, Phys. Rev. B **26**, 2257 (1982).

[6] S. Mochizuki, Phys. Status Solidi B **114**, 189 (1982).

[7] F. Marabelli and P. Wachter, Phys. Rev. B **36**, 1238 (1987).

[8] R. C. Linares, J. Phys. Chem. Solids **28**, 1285 (1967).

[9] T. Suemoto and M. Ishigame, Phys. Rev. B **33**, 2757 (1986).

[10] H. Z. Cummins and P. E. Schoen, in *Laser Handbook*, edited by F. T. Arecchi and E. O. Schulz-DuBois (North-Holland, Amsterdam, 1972).

[11] M. Ishigame and E. Yoshida, Solid State Ionics **23**, 211 (1987).

[12] S. Ganesan and R. Srinivasan, Can. J. Phys. **40**, 74 (1962).

[13] H. Ohura, M. S. thesis, University of Tohoku, 1977.

[14] W. B. Lacina and P. S. Pershan, Phys. Rev. B **1**, 1765 (1970).

[15] M. P. Anderson and A. S. Nowick, J. Phys. (Paris) Colloq. **42**, C5-823 (1981).

[16] M. P. Anderson, D. E. Cox, K. Halperin, and A. S. Nowick, Solid State Ionics **9&10**, 953 (1983).